Quaternary Research (2018), **90**, 127–138.

doi:10.1017/qua.2018.20

A late Quaternary paleoenvironmental record in sand dunes of the northern Atacama Desert, Chile

Kari M. Finstad[a,e]*, Marco Pfeiffer[a,b], Gavin McNicol[a,d,f], Michael Tuite[c], Kenneth Williford[c], Ronald Amundson[a]

[a]Department of Environmental Science, Policy and Management, University of California, Berkeley, California 94720, USA
[b]Departamento de Ingeniería y Suelos, Facultad de Ciencias Agronómicas, Universidad de Chile, Santa Rosa 11315, La Pintana, Chile
[c]Jet Propulsion Laboratory, California Institute of Technology, Pasadena, California 91009, USA
[d]Center for Accelerator Mass Spectrometry, Lawrence Livermore National Laboratory, Livermore, California 94550, USA
[e]Current Address: Center for Accelerator Mass Spectrometry, Lawrence Livermore National Laboratory, Livermore, California 94550, USA
[f]Current address: Alaska Coastal Rainforest Center, University of Alaska Southeast, Juneau, Alaska 99801, USA

(Received September 19, 2017; Accepted February 20, 2018)

Abstract

This paper reports a previously unidentified paleoenvironmental record found in sand dunes of the Atacama Desert, Chile. Long-term aeolian deflation by prevailing onshore winds has resulted in the deposition of sand on the irregular surface of a Miocene-aged anhydrite outcrop. Two deposits ~25 km apart, along the prevailing wind trajectory, were hand excavated then analyzed for vertical (and temporal) changes in physical and chemical composition. Radiocarbon ages of organic matter embedded within the deposits show that rapid accumulation of sediment began at the last glacial maximum and slowed considerably after the Pacific Ocean attained its present post-glacial level. Over this time period, grain sizes are seen to increase while accumulation rates simultaneously decrease, suggesting greater wind speeds and/or a change or decrease in sediment supply. Changes in $\delta^{34}S$ values of sulfate in the sediment beginning ~10 ka indicate an increase in marine sources. Similarly, $\delta^{2}H$ values from palmitic acid show a steady increase at ~10 ka, likely resulting from aridification of the region during the Holocene. Due to the extreme aridity in the region, these sand dunes retain a well-preserved chemical record that reflects changes in elevation and coastal proximity after the last glacial maximum.

Keywords: Hyperarid Atacama Desert; Sand dune; Paleoenvironment; Isotope analyses; Biological soil crust (BSC); Lichen; Fog

INTRODUCTION

The hyperarid Atacama Desert is the driest place on Earth and it has likely maintained a semi-continuously hyperarid climate for millions of years (Hartley and Chong, 2002; Amundson et al., 2012; Jordan et al., 2014). Climate records reconstructed from proxy data suggest increased moisture during the late Pleistocene and progressively drier conditions in the Holocene. Middens, wetlands, and stream activity in northern Chile have been used to reconstruct significant regional late Quaternary wet periods from 17.5–14.2 ka and 13.8–9.7 ka, known as Central Andean Pluvial Events (CAPE; Rech et al., 2002; Nester et al., 2007; Quade et al., 2008; Gayo et al., 2012). Similarly, the occurrence of mollusks in the hyperarid region of southern Peru indicates more humid conditions in the late Pleistocene (Mächtle et al., 2010). Latorre et al. (2011) have suggested that dune deposits in the region may retain records of past climate change, specifically fog intensity. A detailed understanding of the region's climate history is still lacking, however, and additional records are desirable to fully understand the climatic, ecological, and anthropological history of the region.

One of the unique local climate characteristics of this area is the strong and persistent on-shore winds that have sculpted the landscapes in the Llamara Basin and its periphery (Flores-Aqueveque et al., 2012). Within what is largely a deflationary landscape, we found sand dunes that have accumulated in depressions of a highly undulating outcrop of Miocene anhydrite and halite. In this study, we investigated these previously unrecognized deposits to determine whether they accumulate continuously or episodically, and if they preserve a record of environmental change. In addition, we considered the mechanisms that have contributed to the formation of the dunes, and how physical and chemical changes in the sediment may reflect regional environmental changes.

*Corresponding author at: Center for Accelerator Mass Spectrometry, Lawrence Livermore National Laboratory, 7000 East Ave, L-397, Livermore, CA 94550, USA. E-mail address: finstad1@llnl.gov (K.M. Finstad).

METHODS

Site description and sample collection

Two study sites were chosen within the Llamara Basin, a subsection of the endorheic basin of Pampa del Tamarugal. The Llamara Basin is a large semi-enclosed basin that has, over geological time, contained lakes, wetlands, and/or salt accumulations from the evaporation of waters derived from the Andes (Saez et al., 1999; Fig. 1). The various sedimentary outcrops in the Llamara Basin range in age from Miocene to early Holocene. The deposits examined here immediately overlie a Miocene outcrop known as the Soledad Formation. The Soledad Formation is characterized by a several-meter-thick anhydrite (calcium sulfate) cap that overlies many meters of nearly pure halite (sodium chloride; Pueyo et al., 2001). Locally, the anhydrite cap is discontinuous (likely due to aeolian and water erosion), leading to a badland-like topography with closed depressions several meters deep and tens of meters in diameter. In our field area, many of these depressions have been partially infilled with a meter or more of sand. The dunes are now capped by a thin and distinctive lichen-bearing crust in many of these locations (Fig. 2).

The two sites are located along a west-to-east transect on the northern edge of the Soledad Formation at 835 and 895 m above sea level (m asl), and approximately 25 km and 50 km from the Pacific coast (Fig. 1). Both sites experience frequent and strong onshore winds that often bring marine fog.

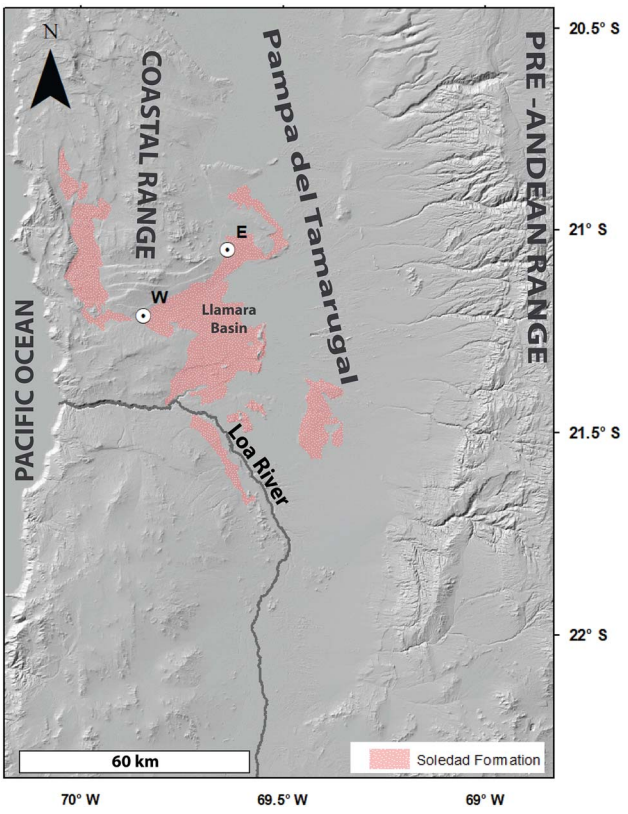

Figure 1. (color online) Location of sites within the Soledad Formation, a sedimentary deposit within the Llamara Basin.

The strong winds clearly result in significant deflation of the regional landscape, creating features such as inverted stream channels, and in other areas (particularly around perennial shrubs and trees), sediment is deposited as coppice dunes (Williams et al., 2017).

In June 2013, one sand dune at each site was hand excavated, and the stratigraphic and pedogenic features were logged and described using standard soil field procedures (Soil Survey Staff, 1999). Samples of each visually observable horizon/strata were collected and transported to the lab in Ziploc bags.

Environmental monitoring

Decagon Devices leaf wetness sensors, Davis cup anemometers, and total solar radiation sensors were used to monitor meteorological conditions at both sites. The leaf wetness sensors were installed as a proxy measurement for fog and dew accumulation (Burgess and Dawson, 2004). Because it did not rain during the year of study, we have assumed that any "wetness" events recorded by the leaf wetness sensors resulted from dew or fog. A value of 460 counts was chosen as the threshold to report wetness, which, according to the manufacturer, is a conservative value. In addition, Onset HOBO Pro v2 (U23-002) temperature and relative humidity sensors were carefully installed beneath sections of lichen crust at each site (Fig. 2). Two sensors were installed at the east site and four sensors were installed at the west site. For all of the sensors, hourly monitoring began June 2013 and ran continuously for 13 months.

Soil chemical and physical characterization

A particle size analysis was performed on each sediment horizon using the hydrometer method outlined by Gee and Bauder (1986). Briefly, excess salt was removed prior to analysis by washing samples with deionized water, and then 30 g of dried sample was dispersed in 100 mL of 5% sodium hexametaphosphate solution by shaking for 16 hours on a horizontal shaker. The suspension was transferred to a sedimentation cylinder and deionized water added to reach 1 L. Contents of the cylinder were mixed thoroughly before the first reading. Readings of each sample and a blank solution were taken at 0.5, 1, 3, 10, 30, 60, 90, 120, and 1440 minutes using the hydrometer. Temperature readings were also taken at each time point.

X-ray diffraction analysis was made on a PANalytical X'Pert Pro diffractometer equipped with a cobalt x-ray tube and X'Celerator detector in the department of Earth and Planetary Science at University of California, Berkeley. Dried samples were prepared for analysis by loading into glass well plates. The material was pressed flat using a glass slide. Each sample was run for 25 minutes.

Sulfate stable isotope ratios

Sulfur stable isotope ratio analysis was performed in the Laboratory for Environmental and Sedimentary Isotope

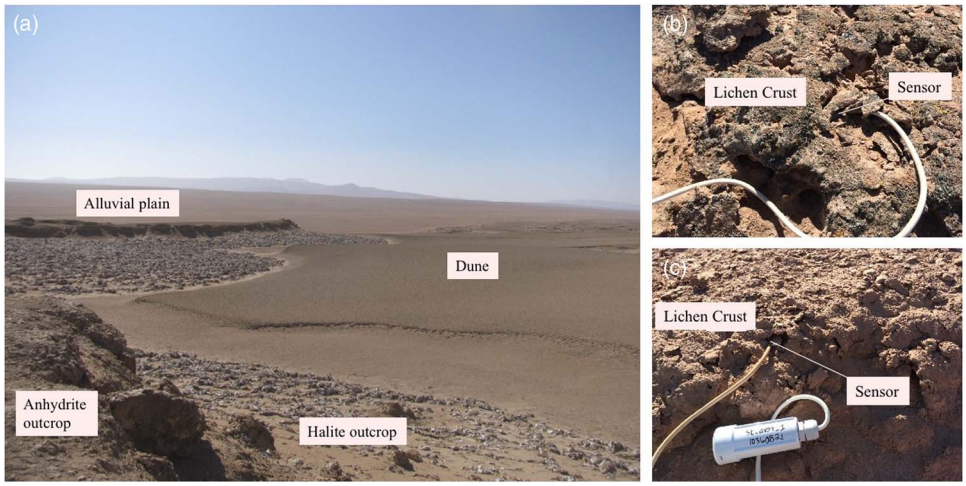

Figure 2. (color online) (a) Landscape of the Soledad Formation demonstrating the rugged terrain and eroded basins now containing sand dunes. Appearance of surface crusts at (b) the west site and (c) east site and installation of temperature and relative humidity sensors.

Geochemistry at the Department of Earth and Planetary Science, University of California, Berkeley, following the protocol outlined in Michalski et al. (2004). Soil sulfate was dissolved in water by shaking pulverized soil for 4 hours in 45 mL deionized water. The mass of soil ranged from 80 to 3000 mg, the sizes needed to precipitate ~100 mg of $BaSO_4$ (based on the total sulfur content of each sample). The sediment was then removed by filtering samples through 0.2 µm filter paper. The sulfate was precipitated as $BaSO_4$ by adding 5 mL 1 M $BaCl_2$ to the solution while samples were in a warm water bath (55°C) under a standard laboratory fume hood. $BaSO_4$ was allowed to precipitate overnight. Samples were then centrifuged at 4000 rpm for 20 minutes and the supernatant was discarded. Precipitated $BaSO_4$ was then dried at 65°C overnight. Approximately 50–200 µg of the $BaSO_4$ sample was analyzed in duplicate on a GV Isoprime isotope ratio mass spectrometer and a Eurovector Elemental Analyzer (EuroEA3028-HT). The analytical precision of the measurement is better than 0.2‰. Values are reported as $\delta^{34}S$ relative to Canyon Diablo Troilite (CDT).

Radiocarbon measurements

Bulk soil samples were prepared for radiocarbon analysis by first removing inorganic carbon and excess salts. Five g of pulverized soil was soaked in 0.5 M HCl for 24 hours with intermittent shaking to agitate the solution, followed by centrifuging and decanting the acidic solution. To ensure complete removal of HCl, the samples underwent alternating soaking and shaking in deionized water for 24 hours, then they were centrifuged and the supernatant discarded. This washing process with deionized water was repeated twice before samples were dried at 60°C.

Radiocarbon analysis was performed on the Van de Graaff FN accelerator mass spectrometer (AMS) at the Center for Accelerator Mass Spectrometry at Lawrence Livermore National Laboratory, Livermore, California. Approximately 0.5 g of washed sample was prepared for ^{14}C measurement by sealed-tube combustion to CO_2 in the presence of CuO and Ag, and then reduced into iron powder in the presence of H_2 at 570°C (Vogel et al., 1984). Aliquots of the CO_2 were analyzed for $\delta^{13}C$ at the Department of Geological Sciences Stable Isotope Laboratory, University of California Davis (GVI Optima Stable Isotope Ratio Mass Spectrometer). Measured $\delta^{13}C$ values were used to correct for mass-dependent fractionation. The AMS precision was 3‰. Radiocarbon ages were calibrated to calendar year BP using the CALIBomb online program (http://calib.qub.ac.uk/CALIBomb/) with the southern hemisphere dataset SH_CAL13 (Hogg et al., 2013) and the 2-sigma probability range is reported. A smoothing of 50 yr was used to account for the gradual growth of lichen and accumulation of organic carbon.

Total fatty acid extraction and GC-IRMS analysis

Fatty acid extraction, esterification, and analysis were performed at the Jet Propulsion Laboratory Astrobiogeochemistry Laboratory (abcLab). Total fatty acids were extracted from the soils and esterified to produce fatty acid methyl esters (FAMEs) following the method developed by Graber and Tsechansky (2010) with a few modifications. Excess salts were first removed from samples from the east site by shaking samples in 250 mL ultrapure (Type 1) water for 4 hours, then the samples were centrifuged and the supernatant discarded. Four g of dried, sieved, and pulverized soil samples were placed in a Teflon tube with $NaSO_4$ added as a desiccant. Six mL of 5% methanolic HCl and 6 mL of toluene were added, the samples vortexed, and then placed in an oven at 60°C overnight. The following day, 15 mL of 5% NaCl solution was added, the samples vortexed, and then centrifuged for 40 minutes at 3000 rpm. The upper organic-bearing phase was pipetted into a new tube and 15 mL of a 2% $KHCO_3$ solution was added. The samples were gently shaken for 2 minutes and then centrifuged for 30 minutes at 3000 rpm. The upper organic-bearing phase was extracted by pipetting and passed over a $NaSO_4$ column then a Si gel

Table 1. Temperature and relative humidity data recorded using Onset HOBO® Pro v2 (U23-002) sensors installed beneath the surface crust (Fig. 2b and c).

Sensor	Max. annual temp. (°C)	Min. annual temp. (°C)	Avg. annual temp. (°C)	Jun–Aug avg temp. (°C)	Sep–Nov avg temp. (°C)	Dec–Feb avg temp. (°C)	Mar–May avg temp. (°C)	Max annual RH (%)	Min annual RH (%)	Avg annual RH (%)	Jun–Aug Avg RH (%)	Sep–Nov Avg RH (%)	Dec–Feb Avg RH (%)	Mar–May Avg RH (%)
W1	43.9	−0.3	17.4	13.6	18.1	22.1	18.2	78.6	7.2	52.1	56.4	46.5	47.7	55.9
W2	46.8	−2.2	17.3	14.4	17.6	20.9	18.1	97.3	3.4	57.4	58.7	53.9	56.1	61.3
W3	52.3	−4.6	19.0	15.3	19.8	23.5	19.8	79.0	6.5	46.9	49.1	42.2	45.1	50.4
W4	52.3	−6.1	17.5	13.1	18.7	23.1	17.9	83.8	4.0	51.1	56	44.4	45.9	55.7
West avg.	48.8	−3.3	17.8	14.1	18.6	22.4	18.5	84.7	5.3	51.9	55.1	46.8	48.7	55.8
E1	54.8	−5.6	19.8	13.8	22.1	27.3	19.9	93.6	5.5	33.1	37.5	24.4	29.7	38.9
E2	62.1	−6.1	20.0	15.6	21.2	25.3	20.5	77.9	3.4	35.0	35.5	28.7	36.1	40.4
East avg.	58.5	−5.8	19.9	14.7	21.7	26.3	20.2	85.7	4.5	34.1	36.4	26.5	32.9	39.6

column. Samples were dried in a stream of N_2 gas and then stored in the freezer at -20°C until analysis. Prior to analysis by GC-MS, samples from the west site were mixed with 100 µL 1:1 *n*-hexane:MTBE solution and samples from the east site mixed with 50 µL 1:1 *n*-hexane:MTBE solution to account for differences in FAME concentration. A procedural blank (pure SiO_2 sand baked at 850°C for 24 hours) was processed with every five unknown samples.

FAME samples were analyzed by GC-MS using a Thermo Trace Ultra GC and ISQ mass spectrometer. The GC was fitted with a 30 m DB-23 column (Agilent 122-2362) using helium as the carrier gas at a constant flow rate of 1 mL/min. The ISQ source was operated at 250°C in EI-mode at 70 eV ionization energy. One µL of sample was injected into a split/splitless injector in splitless mode at 250°C. The GC oven program started at 50°C for two minutes, ramped to 180°C at 15°C/minute, then ramped to 240°C at 10°C/minute and held for 15 minutes. Samples were run in duplicate accompanied by the procedural blanks. The Supelco 37 Component FAME Mix (CRM47885) was injected at least once daily to monitor GC performance and identify FAMEs.

In order to determine the δ^2H of stearic and palmitic acid methyl esters, samples were reanalyzed (also in duplicate) using a Thermo Delta V Plus isotope ratio mass spectrometer coupled to the Trace Ultra GC via a Thermo IsoLink. Analytical conditions were the same as described above except that a fraction of the sample was pyrolized at 1420°C in the IsoLink after eluting from the GC column and was then introduced into the Delta V Plus. Duplicate analyses of Fatty Acid Ester Mixture F8-3 (University of Indiana Isotope Lab) were used to normalize δ^2H values relative to VSMOW. The mean difference between duplicate samples was <4‰. The H3 factor was determined prior to each day's analyses (n = 10) and had a mean value of 5.04 ± 0.13 (1 SD).

RESULTS AND DISCUSSION

Present day meteorological conditions

Leaf wetness sensors were used to measure the present-day differences in fog and dew between the two sites. The data clearly show that the west site receives more intense and frequent fog events. Over the 13 months of recording, the west site had liquid moisture present for 3109 hours, and the east site for 1181 hours, out of 9504 total hours. This is equivalent to the presence of dew ~32% and ~12% of the year at the west and east sites, respectively. The difference in fog occurrence correlates with distance to the coast and elevation, with the western site being ~25 km closer to the coast and 60 m lower in elevation.

Monitoring of the temperature and relative humidity under the surface crust revealed that the west site maintains a higher relative humidity than the east site (Table 1). The average annual relative humidity at the west site was 1.5 times greater than the eastern one (52% versus 34%). This difference in average relative humidity is consistent throughout all

seasons, reflecting the different fog frequencies. The average temperature beneath the crust at the western site was 18°C, and 20°C at the east. The eastern site also has greater temperature extremes, both 10°C warmer and 2.5°C cooler than extremes at the western site.

The anemometers showed that the wind direction was southwest or northeast, and that the western site regularly experiences higher speeds. On average, the wind speeds were 3 m s^{-1} and 1.7 m s^{-1} at the west and east sites, respectively. Both sites experience gusts as high as 11.5 m s^{-1} (Fig. 3).

Location and source of sand dunes

It is increasingly recognized that arid landscapes are complex mosaics of areas impacted by both aeolian deflation and deposition. For example, in the southwestern United States, deflation of exposed playas and stream beds generates dust that accumulates on surrounding landscapes as an aeolian mantle (V horizon) over underlying soils (Turk and Graham, 2011). The Llamara Basin in Chile represents a similar, but more extreme, version of these processes that appear to operate in many deserts.

At the edge of the Soledad Formation are alluvial fans with sulfate-rich soils that have obviously been deflated by wind (Fig. 4). The removal of susceptible soil particles from these surrounding alluvial fans is aided by their relatively low surface roughness. Smooth surfaces facilitate entrained dust particles to remain suspended during transport (Tsoar and Pye, 1987). The rugged topography of the Soledad Formation, however, represents a sharp transition to increased surface roughness.

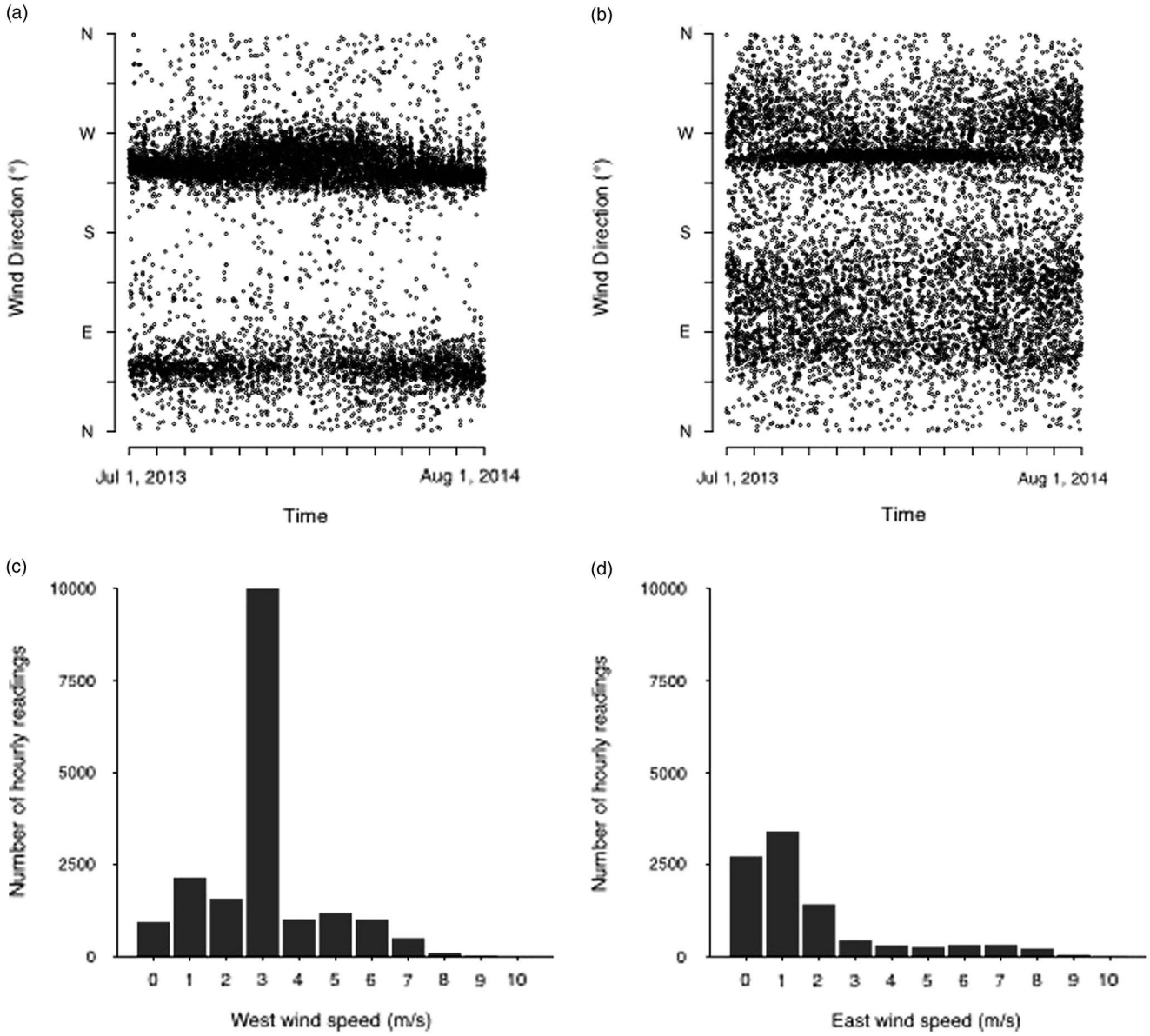

Figure 3. Hourly measurements of wind speed and direction were taken for 13 months beginning in June 2013. Each point represents the wind direction at a single time at the (a) west site and (b) east site. Frequency and range of wind speeds at the (c) west site and (d) east site.

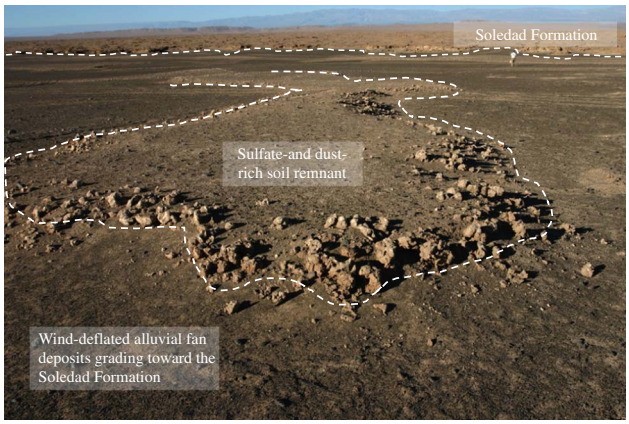

Figure 4. (color online) Wind-deflated alluvial fans grading towards the Soledad Formation presumed to be the source of sand.

This leads to a reduction in wind velocity and a rapid deposition of particles within the Llamara Basin. Deposition does not result in a simple continuous blanket of sand due to the irregularities in the surface and its impact on particle transport. There is a sharp and clear, however, distinction between the generally deflating alluvial fans and sediment deposition within the Soledad Formation.

From the perspective of satellite imagery, a distinctive pattern of the sand dunes emerges (Fig. 5). On the western edge of the Soledad Formation, the deposits are well-developed transverse dunes, oriented slightly to the northwest. Further to the east, the clarity of the dune shape decreases. There, they maintain a less distinct northwest orientation, and, in many areas, the dunes more commonly mimic a star-like orientation. Transverse dunes are oriented perpendicular to the direction of wind flow, while star dunes are believed to form in variable wind trajectories (Anderson and Anderson, 2010), an interpretation which is well aligned with the directions recorded by our anemometers at the west and east sites (Fig. 3).

Dune stratigraphy

The surface of both dunes consists of a thin (cm scale) crust that is solidified by both lichens and sulfate salts. Lichen density was much more distinct in the crust at the western site (Fig. 2b and c). These biological soil crusts comprise an assortment of prokaryotic and eukaryotic organisms (Moore, 1998).

Below the lichen crust, the next 10 to 15 cm of sediment had prominent polygonal structures up to 30 cm in width. With the overlying material removed, these structures appeared to be comprised of smaller polygons in a somewhat fractal-like pattern. Throughout the soil/sedimentary profile are irregularly spaced and somewhat horizontal accumulations of sulfate. Individual soil horizons were thus designated on the basis of changes in the sulfate concentration, color, and bulk density.

The sediment in the dunes is largely silicate in origin (quartz and feldspar) with varying concentrations of sulfate and chloride salts (bassanite, anhydrite, and halite) (Table 2). Carbonate was found only in very low concentrations. At the two sites examined in detail here, the surface layers have bassanite (a partially hydrated sulfate mineral) as the primary sulfate mineral, whereas anhydrite exceeds bassanite in most of the deeper layers. While bassanite is a somewhat uncommon mineral at the Earth's surface, it has been found in evaporite deposits of arid regions on both Earth and Mars (Hunt et al., 1966; Akpokodje, 1984; Gunatilaka et al., 1985; Mees and De Dapper, 2005; Yen et al., 2017). We hypothesize that frequent interactions of the surface minerals with fog favor a more hydrated sulfate species at the immediate land surface, whereas high temperatures and low water activity form and maintain anhydrite at greater soil depths.

Dune accretion

There is little evidence of pedogenesis or physical mixing beneath the surface crust. To test the notion that the dunes have accreted monotonically over time (and have not been physically or biologically mixed), we conducted radiocarbon dating at several depths in both deposits. We found that both profiles show a clear trend of increasing age with increasing depth.

The surface crust at the west site has an average age of 1691 cal yr BP ($n = 4$) and the crust of the east site has an average age of 2573 cal yr BP ($n = 3$). Individual crust samples from the west site have ages of 1614–1780, 1594–1758, 1412–1554, and 1854–1980 cal yr BP, and individual crust samples from the east site have ages of 2514–2778, 2446–2726, and 2370–2692 cal yr BP. Both dunes have late Pleistocene maximum

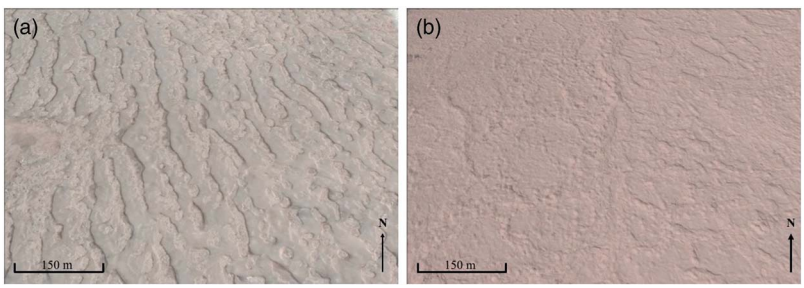

Figure 5. (color online) Satellite image of sites showing the shape of the dunes. (a) On the western edge of the Soledad Formation, the deposits are well-developed transverse dunes, oriented slightly to the northwest. (b) Further to the east, the clarity of the shape of the dunes decreases and the dunes take on a more star-like form. Images were accessed from GoogleEarth in June 2016.

Table 2. Textural classification and most dominant minerals found in each dune layer.

Sample	Depth (cm)	Classification	Sand (%)	Silt (%)	Clay (%)	Mineralogy Most abundant XRD results
West 1	0–2	Loamy Fine Sand	79	13	8	Bassanite, quartz, anhydrite, albite, monalbite
West 2	2–5	Sandy Loam	72	18	10	Anhydrite, quartz, bassanite, albite, muscovite
West 3	5–13	Sandy Loam	68	22	10	Bassanite, quartz, anhydrite, albite
West 4	13–32	Sandy Loam	59	32	9	Anhydrite, quartz, halite, bassanite, sodalite
West 5	32–49	Sandy Loam	66	25	9	Anhydrite, quartz, halite, bassanite, anorthite
West 6	49–67	Sandy Loam	66	26	8	Anhydrite, quartz, halite, bassanite, cristobalite
West 7	67–83	Sandy Loam	73	18	9	Anhydrite, quartz, halite, albite, bassanite
West 8	83–104	Sandy Loam	73	18	9	Anhydrite, quartz, muscovite, bassanite, orthoclase
West 9	104–118	Sandy Loam	64	26	10	Anhydrite, quartz, halite, bassanite, albite
West 10	118–127	Sandy Loam	67	22	11	Bassanite, quartz, anhydrite, halite, albite
West 11	121–149	Sandy Loam	69	21	10	Anhydrite, quartz, halite, albite, bassanite
East 1	0–2	Sandy loam	68	22	10	Bassanite, quartz, anhydrite, sylvine, albite
East 2	2–4	Sandy loam	58	36	6	Bassanite, quartz, anhydrite, albite, muscovite
East 3	4–7	Sandy loam	53	39	8	Anhydrite, quartz, bassanite, albite, muscovite
East 4	7–14	Loam	47	42	11	Anhydrite, quartz, anorthite, bassanite, muscovite
East 5	14–31	Sandy loam	56	35	9	Anhydrite, quartz, albite, halite, bassanite
East 6	31–33	Sandy loam	57	30	13	Quartz, anhydrite, halite, albite, glauberite
East 7	33–52	Sandy loam	54	37	9	Anhydrite, quartz, halite, albite, bassanite

ages at their bases, 18,712–19,246 cal yr BP in the west deposit, and 17,652–18,208 cal yr BP in the eastern one (Table 3; Fig. 6). These dunes therefore represent the somewhat steady accumulation of captured material since the late Pleistocene. The observed increase in age monotonically with depth reflects the absence of biological and physical mixing processes. Due to the hyperarid conditions that have prevailed throughout the formation of these dunes, organic matter has been buried without significant degradation. This has left a preserved record of sedimentation and biologic material.

While the accumulation and growth of the dunes has been monotonic, the rate of growth has not been constant. During the early stages of accumulation, both dunes were growing at a rate of approximately 0.07 cm yr^{-1}. This rate has decreased over time, and both sites are presently growing at rates less than 0.01 cm yr^{-1} (Fig. 7). Given that the magnitude and timing of growth rate changes occur simultaneously at both sites, we conclude that these dunes record a response to regional environmental change occurring during the early Holocene.

Table 3. Radiocarbon ages were calibrated to calendar year BP using the CALIBomb online program (http://calib.qub.ac.uk/CALIBomb/) and using the southern hemisphere dataset SH_CAL13 (Hogg et al., 2013). 2-sigma probability ranges are reported here.

Laboratory ID (CAMS #)	Sample	Depth (cm)	$\delta^{13}C_{org}$ (‰)	Fraction modern	±	^{14}C age (yr BP)	±	Calibrated ^{14}C age (cal yr BP)
164992	West 1	0–2	−22.8	0.7961	0.0025	1830	25	1614–1780
165000	West 1	0–2	−23.1	0.7981	0.0030	1810	35	1594–1758
164994	West 1	0–2	−22.7	0.8154	0.0028	1640	30	1412–1554
164995	West 1	0–2	−22.6	0.7799	0.0023	1995	25	1854–1980
164965	West 3	5–13	−24.5	0.4815	0.0023	5870	40	6514–6742
165882	West 5	32–49	−21.0	0.3090	0.0023	9440	60	10,422–10,776
165160	West 7	67–83	−28.3	0.1469	0.0020	15410	110	18,382–18,852
165883	West 9	104–118	−20.5	0.1329	0.0026	16210	160	19,094–19,952
164993	West 11	121–149	−25.1	0.1409	0.0020	15740	120	18,712–19,246
164996	East 1	0–2	−24.2	0.7211	0.0026	2625	30	2514–2778
165363	East 1	0–2	−23.6	0.7297	0.0022	2530	25	2446–2726
164997	East 1	0–2	−23.3	0.7336	0.0022	2490	25	2370–2692
164998	East 4	7–14	−28.1	0.2270	0.0019	11910	70	13,506–13,846
164999	East 5	14–31	−28.8	0.1642	0.0019	14510	100	17,368–17,918
164966	East 7	33–52	−29.6	0.1589	0.0020	14780	100	17,652–18,208

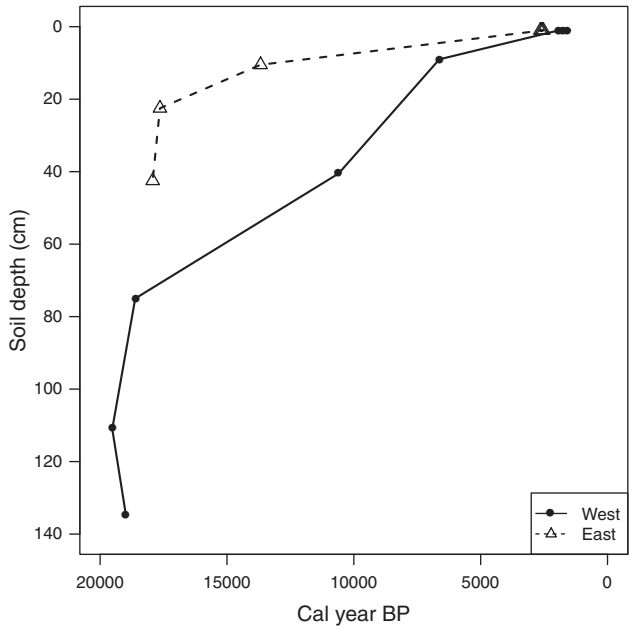

Figure 6. Radiocarbon measurements taken from strata within each dune profile. Additional data can be found in Table 3.

The onset of glacial melting and the subsequent rise in sea level after the last glacial maximum (LGM) began 20 to 19 ka (Yokoyama et al., 2000), shortly before these dunes began accreting. From 19 to 10 ka, sea level rose ~130 m, changing the elevation of our field sites from 965 and 1025 m asl to their present locations at 835 and 895 m asl (Lambeck et al., 2002). This rise in sea level also moved the coastline ~7 km inland, repositioning our sites from 32 and 57 km from the coast to their present locations at 25 and 50 km from the coast. The observed rapid decline in sediment accumulation rates in the dunes examined here coincides with global sea levels approaching modern conditions at 10 ka.

Presently, fog in the Atacama Desert seldom penetrates regions above 1000 m asl (Rech et al., 2003; Cereceda et al., 2002; Houston, 2006). It is therefore probable that fog intensity and frequency at our field areas were significantly lower during the LGM than they are today, given the increased elevations and distance from the coast. The lower sea level may have exposed expanses of shelf for wind deflation and the decreased fog intensity may have weakened soil surface crusts and made sulfate-rich soils on alluvial fans and uplands more susceptible to deflation. As a starting hypothesis, prior to examining the chemical and isotopic records in the sediment, we propose that the observed changes in sand deposition rates are in response to changes in sea level, corresponding to an increase in wind speeds and fog density, resulting in a decrease in the rate of sand deposition.

Paleoenvironmental records in the dunes

Textural analysis of the sediment

Nearly all of the sediment in the dunes has a textural classification of a sandy loam, though strata at the west site constantly have a larger grain size (more sand) relative to the east site (Table 2; Fig. 8). As previously discussed, wind speeds at the west site are ~2× higher than those at the east site. This difference in wind speed creates a spatial gradient with grain size decreasing further from the coast as the capacity for transporting larger grain sizes decreases.

Prior to 15 ka, the grain size accumulating at each site was relatively constant (though coarser at the west site). After this time, both sites reveal a steady increase in the proportion of

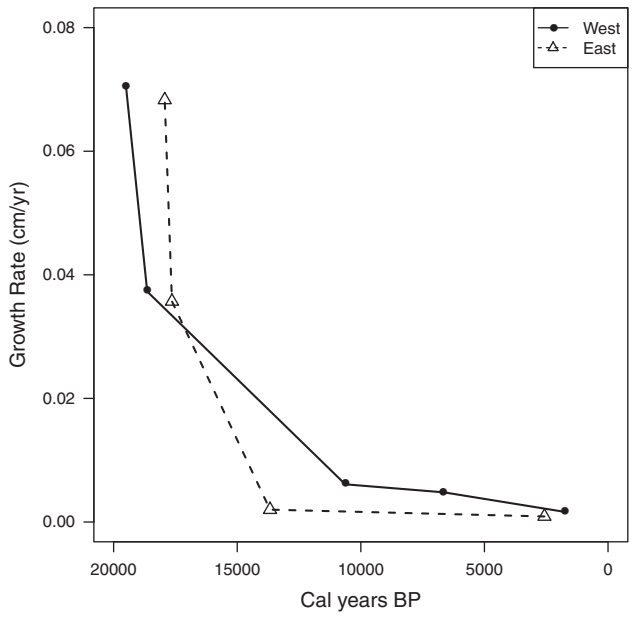

Figure 7. Rate of dune accretion calculated using radiocarbon ages in Figure 6 and Table 3.

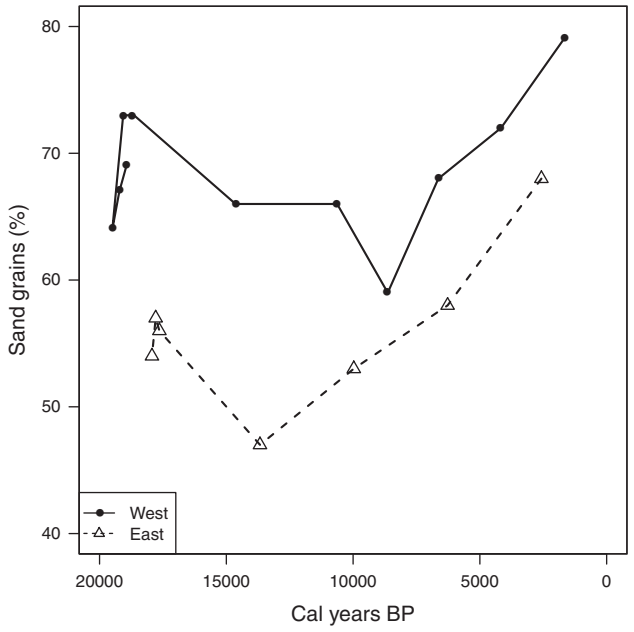

Figure 8. Changes in sediment grain size at both sites over time. Additional data can be found in Table 2.

sand grains. We interpret this as a reflection of changes in coastal proximity and/or wind speeds linked to changes in sea level. The timing of this change coincides with the observed decrease in dune accumulation rate. Rising sea level and increasing wind speeds could both increase the size of grains transported and simultaneously increase erosion from the dunes, leading to the observed decrease in accumulation rates and increase in grain size.

Stable isotope ratios of sulfur in sulfate

The $\delta^{34}S$ values of the sulfate at both sites does not vary widely, averaging +8.5 ± 0.2‰ at the west site and + 9.1 ± 0.4‰ at the east site (Table 4; Fig. 9). Possible sulfate sources to these sites include: (1) deflated sulfate rich soils from nearby alluvial fans, (2) erosion and deflation of anhydrite from the Soledad Formation, (3) deflation of evaporitic sulfate from nearby salars, and (4) various marine inputs. Rech et al. (2003) reported that Andean rocks have $\delta^{34}S$ values of -5 to +5‰, and here we report values of +6‰ for the anhydrite in the Soledad Formation. Finstad et al. (2016) reported values of +5.5‰ for groundwater sulfate and +2.7 and +5.1‰ of evaporitic sulfate on the surface of nearby salars. In contrast, Bao et al. (2000) has reported that biogenic marine sulfates have $\delta^{34}S$ values ranging from +13 to +22‰, and seawater sulfate a $\delta^{34}S$ value of about +21‰. Given these values, both sites are likely receiving the majority of their sulfate from some combination of Andean sources (ancient Soledad Formation, salars, and/or local soil sulfate) and minor marine inputs.

A shift in the isotopic composition of the sulfate, primarily at the east site, began roughly 10 ka. At this time, $\delta^{34}S$ values begin to steadily increase, suggesting a larger input of marine sulfates (although the total amount remained small). While the change is small, it coincides to the time when other data discussed earlier suggest an increase in local wind speeds and rising sea level after the LGM. Changes in coastal proximity may have facilitated larger contributions of marine material to these deposits, leading to the observed increase in the $\delta^{34}S$ sulfate values.

Table 4. Measured stable isotope data from each dune layer.

Sample	Depth (cm)	$\delta^{34}S$ sulfate (‰, CDT)	$\delta^{2}H$ Palmitic Acid (‰, VSMOW)	$\delta^{15}N$ org N (‰, air)
West 1	0–2	8.54	–88.2	1.59
West 1	0–2	8.69	–85.2	1.48
West 2	2–5	8.77	–98.3	1.68
West 2	2–5	8.74	–103	1.98
West 3	5–13	8.73	–134.3	3.20
West 3	5–13	8.30	–136.5	3.27
West 4	13–32	8.44	–167	4.24
West 4	13–32	8.35	–166.7	4.43
West 5	32–49	8.39	–148.2	3.34
West 5	32–49	8.67	–145.5	3.24
West 6	49–67	8.60	–155.7	4.35
West 6	49–67	8.36	–150.1	4.47
West 7	67–83	8.37	–	7.30
West 7	67–83	8.50	–	7.17
West 8	83–104	8.43	–	6.46
West 8	83–104	8.44	–	6.40
West 9	104–118	8.32	–147.9	3.25
West 9	104–118	8.43	–146.2	3.17
West 10	118–127	8.27	–138.8	2.36
West 10	118–127	8.43	–133.4	2.63
West 11	121–149	8.19	–137	7.16
West 11	121–149	8.49	–142	6.42
East 1	0–2	9.89	–60.6	8.59
East 1	0–2	9.68	–62.2	7.70
East 2	2–4	9.59	–91.2	5.75
East 2	2–4	9.37	–90.7	7.02
East 3	4–7	8.87	–114.8	8.51
East 3	4–7	8.79	–111.6	7.47
East 4	7–14	8.89	–127.2	11.00
East 4	7–14	8.82	–123.6	11.57
East 5	14–31	9.13	–136.5	11.79
East 5	14–31	8.88	–134.7	11.96
East 6	31–33	8.93	–138.2	12.47
East 6	31–33	8.93	–137	13.07
East 7	33–52	8.80	–148.2	16.25
East 7	33–52	8.61	–144.5	16.65

Stable isotope ratios of hydrogen in fatty acids

The use of $\delta^{2}H$ values in lipid biomarkers as a paleoclimate proxy is becoming increasingly common (e.g., Andersen et al., 2001; Sauer et al., 2001;Huang et al., 2002; Sachse et al., 2004). The basis for the approach is that photosynthetic organisms derive H from water sources, therefore the $\delta^{2}H$ in their lipids reflects the $\delta^{2}H$ of the source water plus a biochemically mediated isotope fractionation. Here we focus

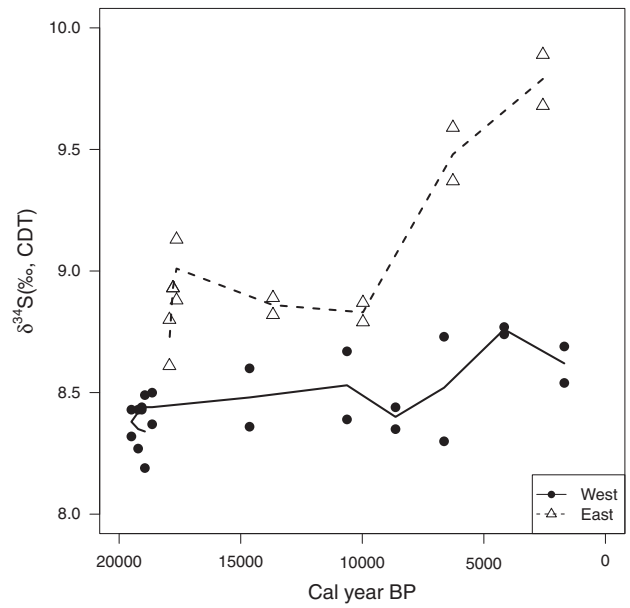

Figure 9. Measured $\delta^{34}S$ values from extractable sulfate at both sites over time. All values are reported relative to Canyon Diablo Troilite (CDT). Additional data in Table 4.

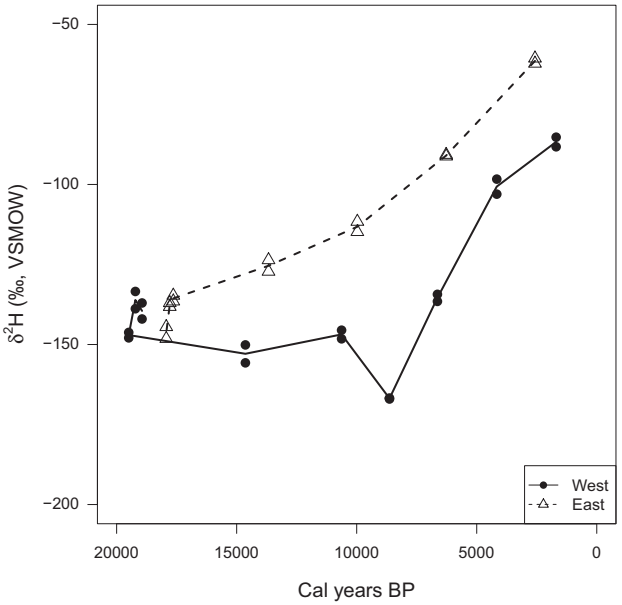

Figure 10. Measured δ^2H values in palmitic acid at both sites over time. All values are reported relative to Vienna Standard Mean Ocean Water (VSMOW). Additional data in Table 4.

on palmitic acid, one of the most common fatty acids in microorganisms, plants, and animals. In both dunes, the δ^2H value of palmitic acid at the base is close to -140‰. Values of δ^2H increase with time, reaching -87‰ and -61‰ at the surface of the west and east sites, respectively (Table 4; Fig. 10). After roughly 17.5 ka, the lipids at the east site are consistently 30 to 50‰ enriched in ^2H relative to the west site.

The H isotope fractionation between water and fatty acids during lipid biosynthesis is reported to range from −170 to −226‰, with a mean value of −200‰ (Sessions et al., 1999). Present-day coastal fog measured ~1000 km south of our field sites is reported to range from −1 to −10‰, with a mean value of −3.4‰ (Aravena et al., 1989). Lipids formed from this fog water experiencing a −200‰ fractionation would have a δ^2H of −203.4‰. This is significantly more ^2H-depleted than the lipids measured at the surface of the dunes.

Three key processes may affect the H isotopic composition of advection fog. First, as fog travels inland and begins to condense and dissipate with westerly winds, the fog vapor will become progressively ^2H-depleted as the heavier isotopologue condenses out in droplets. Second, as the fog rises and warms as it crosses the continent, it will undergo preferential evaporation of ^1H_2O, resulting in fog with a higher δ^2H relative to the starting fog. Finally, after the fog deposition, additional ^2H enrichment may occur via evaporation from the land surface prior to biologic incorporation.

We suggest that the latter two processes dominate the landscape considered here and can explain the consistent difference in δ^2H values between the west and east sites. The meteorological data indicate that the east site is 1.5 to 2.5 times less humid and foggy than the west (Table 1), which is further supported by visual observations of fog intensity in the field. Fog reaching the east site has likely undergone evaporative enrichment both during transport and after deposition on the landscape, resulting in consistently higher δ^2H values from lipids at the east site. The δ^2H in lipids at both sites increases over time, with the trend becoming most pronounced ~10 ka. We suggest that the observed pattern may be due to aridification of the region during the Holocene. Increasing temperatures and deceasing humidity would have led to a steady increase in evaporative enrichment of the fog at both sites prior to deposition.

CONCLUSION

Here, we report the discovery of small-scale late Quaternary sand dunes in a windy and fog-impacted region of the Atacama Desert. The unique accumulation of sediment has apparently occurred in response to a combination of sea level and advective fog changes that occurred from the late Pleistocene to Holocene. The dunes have accumulated in a rugged, badland-type topography that causes local variations and reductions in wind velocity, and subsequent settling of suspended particles from the surface winds. Radiocarbon ages of organic matter embedded within the deposits show that they began accumulating rapidly at the LGM, and that accumulation of sediment slowed considerably after the Pacific Ocean attained its present post-glacial level.

Due to the extreme aridity and lack of biological mixing processes, the dunes retain a detailed stratigraphic record of chemical and physical changes over the last 20 ka. Chemical and isotopic analysis of the sediment and fatty acids preserved within the dunes likely reflect elevation and coastal proximity changes following the last glacial maximum. Over this time period, grain sizes are seen to increase while accumulation rates simultaneously decrease, suggesting greater wind speeds and/or a decrease in sediment supply. Changes in $\delta^{34}S$ values of the sediment beginning ~10 ka indicate an increase in marine influence, likely as fog, or slight changes in the source of the sulfate. Similarly, δ^2H values from palmitic acid show a steady increase ~10 ka, likely resulting from increased aridity in the region during the Holocene.

This unique and continuous record of paleoenvironmental conditions provides a window into local processes that are impacted by a complex array of sea level, marine upwelling, and fog processes. The depth-increment sampling conducted here was relatively coarse in order to test whether the sediments in the dunes indeed had accumulated monotonically. It appears that much finer scale depth increments coupled with radiocarbon dating could provide a higher resolution late Quaternary record.

ACKNOWLEDGMENTS

We are grateful for the following support: funding to K.F. through the NASA Earth and Space Sciences Fellowship and NSF Doctoral Dissertation Improvement Grant (DEB-1406956); to M.P. through the CONICYT for Becas Chile Scholarship and the Fulbright Foreign Student Program Scholarship; and to R.A. through the

University of California Agricultural Experiment Station and National Science Foundation grant # 0819972. Kim Lychens is thanked for her help with the fatty acid extractions. Part of this research was done at the Jet Propulsion Laboratory, California Institute of Technology, under a grant from the National Aeronautics and Space Administration. A portion of this work was performed under the auspices of the U.S. Department of Energy by Lawrence Livermore National Laboratory under Contract DE-AC52-07NA27344, LLNL-JRNL-717742.

REFERENCES

Akpokodje, E., 1984. The occurrence of bassanite in some Australina arid zone soils. *Chemical Geology* 47, 361–364.

Amundson, R., Dietrich, W.E., Bellugi, D.G., Ewing, S.A., Nishiizumi, K., Chong, G.D., Owen, J., et al., 2012. Geomorphologic evidence for the late Pliocene onset of hyperaridity in the Atacama Desert. *Geological Society of America Bulletin* 124, 1048–1070.

Andersen, N., Paul, H., Bernasconi, S., McKenzie, J., Behrens, A., Schaeffer, P., Albrecht, P., 2001. Large and rapid climate variability during the Messinian salinity crisis: evidence from deuterium concentrations of individual biomarkers. *Geology* 29, 799–802.

Anderson, R.S., Anderson, S.P., 2010. *Geomorphology: The Mechanics and Chemistry of Landscapes*. Cambridge University Press, Cambridge, United Kingdom.

Aravena, R., Suzuki, O., Pollastri, A, 1989. Coastal fog and its relation to groundwater in the IV region of northern Chile. *Chemical Geology* 79, 83–91.

Bao, H., Campbell, D.A., Bockheim, J.G., Thiemens, M.H., 2000. Origins of sulphate in Antarctic Dry-Valley soils as deduced from anomalous ^{17}O compositions. *Nature* 407, 499–502.

Burgess, S.S.O., Dawson, T.E., 2004. The contribution of fog to the water relations of Sequoia smpervirens (D. Don): foliar uptake and prevention of dehydration. *Plant, Cell and Environment* 27, 1023–1034.

Cereceda, P., Osses, P., Larrain, H., Farías, M., Lagos, M., Pinto, R., Schemenauer, R.S., 2002. Advective, orographic and radiation fog in the Tarapacá region, Chile. *Atmospheric Research* 64, 261–271.

Finstad, K., Pfeiffer, M., McNicol, G., Barnes, J., Demergasso, C., Chong, G., Amundson, R., 2016. Rates and geochemical processes of soil and salt crust formation in salars of the Atacama Desert, Chile. *Geoderma* 284, 57–72.

Flores-Aqueveque, V., Alfaro, S. C., Caquineau, S., Foret, G., Vargas, G., Rutllant, J. A., 2012. Inter-annual variability of southerly winds in a coastal area of the Atacama Desert: implications for the export of aeolian sediments to the adjacent marine environment. *Sedimentology* 59, 990–1000.

Gayo, E.M., Latorre, C., Jordan, T.E., Nester, P.L., Estay, S.A., Ojeda, K.F., Santoro, C.M., 2012. Late Quaternary hydrological and ecological changes in the hyperarid core of the northern Atacama Desert (~21°S). *Earth Science Reviews* 113, 120–140.

Gee, G., Bauder, J., 1986. Particle-size analysis. In: Klute, A. (Ed.), *Methods of Soil Analysis: Part 1—Physical and Mineralogical Methods,* SSSA Book Series 5.1. American Society of Agronomy, Inc. (ASA) and Soil Science Society of America, Inc. (SSSA). Madison, Wisconsin, pp. 383–411.

Graber, E.R., Tsechansky, L., 2010. Rapid one-step method for total fatty acids in soils and sediments. *Soil Science Society of America Journal* 74, 42–50.

Gunatilaka, A., Al-Temeemi, A., Saleh, A., Nassar, N., 1985. A new occurrence of bassanite in recent evaporitic environments, Kuwait, Arabian Gulf. *Kuwait Journal of Science* 12, 157–166.

Hartley, A., Chong, G.D., 2002. Late Pliocene age for the Atacama Desert: implications for the desertification of western South America. *Geology* 30, 43–46.

Hogg, A., Hua, Q., Blackwell, P., Niu, M., Buck, C., Guilderson, T.P., Heaton, T.H.E., et al., 2013. SHCAL13 southern hemisphere calibration, 0–50,000 years cal BP. *Radiocarbon* 55, 1889–1903.

Houston, J., 2006. Evaporation in the Atacama Desert: an empirical study of spatio-temporal variations and their causes. *Journal of Hydrology* 330, 402–412.

Huang, Y., Shuman, B., Wang, Y., Webb, T.I., 2002. Hydrogen isotope ratios of palmitic acid in lacustrine sediments record late Quaternary climate variations. *Geology* 12, 1–4.

Hunt, C., Robinson, T., Bowles, W., Washburn, A., 1966. Hydrologic basin Death Valley California. Geological Survey Professional Paper 494-B, US Government Printing Office, Washington, DC.

Jordan, T.E., Kirk-Lawlor, N.E., Blanco, N., Rech, J.A., Cosentino, N.J., 2014. Landscape modification in response to repeated onset of hyperarid paleoclimate states since 14 Ma, Atacama Desert, Chile. *Geological Society of America Bulletin* 126, 1016–1046.

Lambeck, K., Yokoyama, Y., Purcell, T., 2002. Into and out of the Last Glacial Maximum: sea-level change during Oxygen Isotope Stages 3 and 2. *Quaternary Science Reviews* 21, 343–1360.

Latorre, C., González, A., Quade, J., Fariña, J., Pinto, R., Marqet, P., 2011. Establishment and formation of fog-dependent Tillandsia landbeckii dunes in the Atacama Desert: evidence from radiocarbon and stable isotopes. *Journal of Geophysical Research* 116, G03033. http://dx.doi.org/10.1029/2010JG001521.

Mees, F., De Dapper, M., 2005. Vertical variations in bassanite distribution patterns in near-surface sediments, southern Egypt. *Sedimentary Geology* 181, 225–229.

Michalski, G., Bohlke, J.K., Thiemens, M.H., 2004. Long term atmospheric deposition as the source of nitrate and other salts in the Atacama Desert, Chile: new evidence from mass-independent oxygen isotopic compositions. *Geochimica et Cosmochimica Acta* 68, 4023–4038.

Moore, P.D., 1998. Life in the upper crust. *Nature* 393, 419–420.

Mächtle, B., Unkel, I., Eitel, B., Kromer, B., Schiegl, S., 2010. Molluscs as evidence for a late Pleistocene and early Holocene humid period in the southern coastal desert of Peru (14.5°S). *Quaternary Research* 73, 39–47.

Nester, P.L., Gayo, E.M., Latorre, C., Jordan, T.E., Blanco, N., 2007. Perennial stream discharge in the hyperarid Atacama Desert of northern Chile during the latest Pleistocene. *Proceedings of the National Academy of Sciences* 104, 19724–19729.

Pueyo, J.J., Chong, G.D., Jensen, A., 2001. Neogene evaporites in desert volcanic environments: Atacama Desert, northern Chile. *Sedimentology* 48, 1411–1431.

Quade, J., Rech, J.A., Betancourt, J.L., Latorre, C., Quade, B., Rylander, K.A., Fisher, T., 2008. Paleowetlands and regional climate change in the central Atacama Desert, northern Chile. *Quaternary Research* 69, 343–360.

Rech, J.A., Quade, J., Betancourt, J.L., 2002. Late Quaternary paleohydrology of the central Atacama Desert (lat 22-24 S), Chile. *Geological Society of America Bulletin* 114, 334–348.

Rech, J.A., Quade, J., Hart, W.S., 2003. Isotopic evidence for the source of Ca and S in soil gypsum, anhydrite and calcite in the Atacama Desert, Chile. *Geochimica et Cosmochimica Acta* 67, 575–586.

Sachse, D., Radke, J., Gleixner, G., 2004. Hydrogen isotope ratios of recent lacustrine sedimentary n-alkanes record modern climate variability. *Geochimica et Cosmochimica Acta* 68, 4877–4889.

Sáez, A., Cabrera, L., Jensen, A., Chong, G., 1999. Late Neogene lacustrine record and palaeogeography in the Quillagua-Llamara basin, Central Andean fore-arc (northern Chile). *Palaeogeography, Palaeoclimatology, Palaeoecology* 151, 5–37.

Sauer, P., Eglinton, T.I., Hayes, J.M., Schimmelmann, A., Sessions, A.L., 2001. Compound-specific D/H ratios of lipid biomarkers from sediments as a proxy for environmental and climatic conditions. *Geochimica et Cosmochimica Acta* 65, 213–222.

Sessions, A.L., Burgoyne, T., Schimmelmann, A., Hayes, J.M., 1999. Fractionation of hydrogen isotopes in lipid biosynthesis. *Organic Geochemistry* 30, 1193–1200.

Soil Survey Staff, 1999. *Soil Taxonomy: A Basic System of Soil Classification for Making and Interpreting Soil Surveys*. 2nd ed. United States Department of Agriculture Handbook 436. Natural Resources Conservation Service.

Tsoar, H., Pye, K., 1987. Dust transport and the question of desert loess formation. *Sedimentology* 34, 139–153.

Turk, J.K., Graham, R.C., 2011. Distribution and properties of vesicular horizons in the western United States. *Soil Science Society of America Journal* 75, 1449.

Vogel, J.S., Southon, J., Nelson, D.E., Brown, T.A., 1984. Performance of catalytically condensed carbon for use in accelerator mass spectrometry. *Nuclear Instruments and Methods in Physics Research*, 289–293.

Williams, R.M.E., Chuang, F.C., Berman, D.C., 2017. Multiple surface wetting events in the greater Meridiani Planum region, Mars: evidence from valley networks within ancient cratered highlands. *Geophysical Research Letters* 44. http://dx.doi.org10.1002/2016GL072259.

Yen, A.S., Ming, D.W., Vaniman, D.T., Gellert, R., Blake, D.F., Morris, R.V., Morrison, S.M., et al., 2017. Multiple stages of aqueous alteration along fractures in mudstone and sandstone strata in Gale Crater, Mars. *Earth and Planetary Science Letters* 471, 186–198.

Yokoyama, Y., Lambeck, K., De Deckker, P., Johnston, P., Fifield, L.K., 2000. Timing of the Last Glacial Maximum from observed sea-level minima. *Nature* 406, 713–716.